



HAL
open science

Exoplanet detection in angular and spectral differential imaging: local learning of background correlations for improved detections

Olivier Flasseur, Loic Denis, Éric Thiébaud, Maud Langlois

► To cite this version:

Olivier Flasseur, Loic Denis, Éric Thiébaud, Maud Langlois. Exoplanet detection in angular and spectral differential imaging: local learning of background correlations for improved detections. Adaptive Optics Systems VI, Jun 2018, Austin, United States. pp.101, 10.1117/12.2313601 . hal-04695072

HAL Id: hal-04695072

<https://hal.science/hal-04695072v1>

Submitted on 11 Sep 2024

HAL is a multi-disciplinary open access archive for the deposit and dissemination of scientific research documents, whether they are published or not. The documents may come from teaching and research institutions in France or abroad, or from public or private research centers.

L'archive ouverte pluridisciplinaire **HAL**, est destinée au dépôt et à la diffusion de documents scientifiques de niveau recherche, publiés ou non, émanant des établissements d'enseignement et de recherche français ou étrangers, des laboratoires publics ou privés.

Exoplanet detection in angular and spectral differential imaging: local learning of background correlations for improved detections

Olivier Flasseur^a, Loïc Denis^a, Éric Thiébaud^b, and Maud Langlois^b

^aUniversité de Lyon, UJM Saint-Etienne, CNRS, Institut d'Optique Graduate School, Laboratoire Hubert Curien UMR 5516, F-42023, Saint-Etienne, France

^bUniversité de Lyon, Université Lyon1, ENS de Lyon, CNRS, Centre de Recherche Astrophysique de Lyon UMR 5574, F-69230, Saint-Genis-Laval, France

ABSTRACT

The search for new exoplanets by direct imaging is a very active research topic in astronomy. The detection is particularly challenging because of the very high contrast between the host star and the companions. They thus remain hidden by a nonstationary background displaying strong spatial correlations. We propose a new algorithm named PACO (for PATCH COvariances) for reduction of differential imaging datasets. Contrary to existing approaches, we model the background correlations using a local Gaussian distribution that locally captures the spatial correlations at the scale of a patch of a few tens of pixels. The decision in favor of the presence or the absence of an exoplanet is then performed by a binary hypothesis test. The method is completely parameter-free and produces both stationary and statistically grounded detection maps so that the false alarm rate, the probability of detection and the contrast can be directly assessed without postprocessing and/or Monte-Carlo simulations. We describe in a forthcoming paper its detailed principle and implementation. In this paper, we recall the principle of the PACO algorithm and we give new illustrations of its benefits in terms of detection capabilities on datasets from the VLT/SPHERE-IRDIS instrument. We also apply our algorithm on multi-spectral datasets from the VLT/SPHERE-IFS spectrograph. The performance of PACO is compared to state-of-the-art algorithms such as TLOCI and KLIP-PCA.

Keywords: direct imaging, angular and spectral differential imaging, data reduction, processing algorithm, statistical method

1. INTRODUCTION

Direct imaging¹ is a recent and very effective technique for the characterization of young and massive objects.² The very high contrast (typically higher than 10^5 in the near infrared) between the host star and its companions makes the detection particularly challenging.^{3,4} In addition to the use of an extreme adaptive optics system and a coronagraph to strongly attenuate the flux from the star,^{5,6} dedicated processing methods that combine images taken while the field of view is rotated (*i.e.* in angular differential imaging mode) and at several wavelengths are required. The different temporal behaviors of the remaining stellar leakages and of the signal originating from the exoplanets make it possible to recover them separately, and thus detect the exoplanets and estimate their astrometry and photometry.

The cutting-edge planet-finder SPHERE⁷ (Spectro-Polarimetry High-contrast Exoplanet REsearch) currently operating at the VLT (Very Large Telescope) provides 4D spatio-temporo-spectral datacubes. Its differential imager IRDIS⁸ (InfraRed Dual Imaging Spectrograph) is optimized for imaging exoplanets at two different wavelengths. A finer characterization of the exoplanet candidates can be made with the integral fields spectrographs (IFS). From a signal processing point of view, a major difficulty in the data analysis comes from the strong spatial and temporal fluctuations of the background that are due to (i) the speckle patterns (originating from the

E-mail: olivier.flasseur@univ-st-etienne.fr ; loic.denis@univ-st-etienne.fr

residual phase aberrations), and (ii) the detection noise and other noise sources (thermal background, flat field error, bad pixels) that are correlated by the interpolations performed by conventional prereduction pipelines.⁹

Generally, images are combined following a particular strategy based on angular and/or spectral differences^{10,11} such as in the TLOCI-type algorithms^{12–16} or by splitting the data into different components (or subspaces) such as in the KLIP-PCA¹⁷ standard or in the LLSG¹⁸ algorithm. In all these techniques, it is in practice difficult to set detection threshold at a given probability of false alarms (more false alarms are observed than expected using a conventional 5σ threshold). Another family of methods is based on a more rigorous statistical framework using maximum likelihood approach such as in the ANDROMEDA^{19,20} and MOODS²¹ algorithms. A more recent method²² exploits supervised machine learning algorithms to detect the typical signature of an exoplanet in science data. However, in all of these techniques the number of tuning parameters stays important making the optimality difficult to reach. The intervention of an expert is thus mandatory to conclude on the confidence level of potential detections.

We propose to follow a different statistical approach with our algorithm PACO (for PATCH COvariances): we model the correlations of the background signal (noise+speckles) in the data with a local Gaussian distribution that captures the spatial correlations at the scale of a patch of a few tens of pixels. The decision in favor of the presence or the absence of an exoplanet is then performed by a binary hypothesis test. This local modeling accounts for the spatial variations of the background fluctuations and leads to a detection method that is completely parameter-free. Moreover, we perform a joint estimation of the flux of each detected source and of the background statistics to provide an intrinsically unbiased photometric estimation.

Based on our forthcoming methodological paper,²³ we recall in section 2 the principle of PACO for angular differential imaging. Section 3 illustrates PACO on datasets from the VLT/SPHERE-IRDIS instrument emphasizing its automatic adaptativity regardless of the considered dataset. In section 4, we extend PACO to spectral datacubes by independently processing each spectral channel of a VLT/SPHERE-IFS dataset. The detection maps from each spectral channel can then be combined into a single detection map. Section 5 concludes the paper.

2. PACO: EXOPLANET DETECTION IN ANGULAR DIFFERENTIAL IMAGING BASED ON PATCH COVARIANCES

2.1 Exoplanet Detection and Flux Estimation with the PACO Algorithm

We consider ADI datasets made of T N -pixels temporal frames in which the field of view undergoes a known motion with respect to background speckles. PACO is based on locally learning a model of the background from the collection of T spatial patches extracted at a given spatial location.

By denoting ϕ_0 the initial 2D location of an exoplanet in a reference frame and $\phi_t = \mathcal{F}_t(\phi_0)$ its location in frame t ($\phi_t \neq \phi_0$ due to field-of-view rotation in ADI), we model the intensity r_{θ_k, t_ℓ} at the 2D angular location θ_k and a the time t_ℓ by the superimposition a background component and an off-axis point spread function (PSF):

$$r_{\theta_k, t_\ell} = f_{\theta_k, t_\ell} + \alpha h_{\theta_k}(\phi_{t_\ell}), \quad (1)$$

with $\alpha > 0$ the flux of the source located at ϕ_0 (e.g., an exoplanet) and $\alpha = 0$ in the absence of source at ϕ_0 , $h_{\theta_k}(\phi_{t_\ell}) = h(\theta_k - \phi_{t_\ell})$ the off-axis PSF, centered on the location ϕ_{t_ℓ} of the exoplanet at time t_ℓ and sampled at pixel location θ_k . The background f_{θ_k, t_ℓ} at spatio-temporal index (k, ℓ) accounts for the stellar leakages and for the different sources of noise. Using a maximum likelihood approach, the estimator of the flux α of an exoplanet located at ϕ_0 in the reference frame is:

$$\hat{\alpha} = \arg \max_{\alpha} p_f(\{r_{\theta_k, t_\ell} - \alpha h_{\theta_k}(\mathcal{F}_{t_\ell}(\phi_0))\}_{k=1:N, \ell=1:T}), \quad (2)$$

where p_f denotes the likelihood of the background term f . Within this statistical framework, the detection can be expressed by the binary hypothesis test:

$$\begin{cases} \mathcal{H}_0 : \{r_{\theta_k, t_\ell}\}_{\ell=1:T, k=1:N} = \{f_{\theta_k, t_\ell}\}_{\ell=1:T, k=1:N} \\ \mathcal{H}_1 : \{r_{\theta_k, t_\ell}\}_{\ell=1:T, k=1:N} = \{f_{\theta_k, t_\ell}\}_{\ell=1:T, k=1:N} + \alpha \{h_{\theta_k}(\phi_{t_\ell})\}_{\ell=1:T, k=1:N} \end{cases} \quad (3)$$

Literally, under \mathcal{H}_0 hypothesis, the observed intensity is only pure background while an exoplanet of flux $\alpha > 0$ is present under \mathcal{H}_1 hypothesis. The detection can be made via the generalized likelihood ratio test (GLRT):²⁴

$$\log \frac{\text{P}_f(\{r_{\theta_k, t_\ell} - \hat{\alpha} h_{\theta_k}(\phi_{t_\ell})\}_{k=1:N, \ell=1:T})}{\text{P}_f(\{r_{\theta_k, t_\ell}\}_{k=1:N, \ell=1:T})} \underset{\mathcal{H}_0}{\overset{\mathcal{H}_1}{\geq}} \eta. \quad (4)$$

A statistical model of the background is then necessary to decide if a detection is relevant or not and estimate the potential exoplanet flux using equations (2) and (4). Contrary to existing approaches^{13, 17, 20} aiming to whiten the background samples using dedicated preprocessings, the PACO modeling takes into account the spatial correlations of the data. Given the nonstationarity of the background in the field of view, the random fluctuations of the background at location θ_k are captured using a multi-variate Gaussian model $\mathcal{N}(\mathbf{m}_{\theta_k}, \mathbf{C}_{\theta_k})$ from the patches collection $\{\mathbf{f}_{\theta_k, t_\ell}\}_{\ell=1:T}$ centered at the location θ_k . The mean and covariance can be estimated from the observed patches using the maximum likelihood estimators:

$$\hat{\mathbf{S}}_{\theta_k} = \frac{1}{T} \sum_{\ell=1}^T (\mathbf{r}_{\theta_k, t_\ell} - \hat{\mathbf{m}}_{\theta_k}) \cdot (\mathbf{r}_{\theta_k, t_\ell} - \hat{\mathbf{m}}_{\theta_k})^t \quad \text{with} \quad \hat{\mathbf{m}}_{\theta_k} = \frac{1}{T} \sum_{\ell=1}^T \mathbf{r}_{\theta_k, t_\ell}, \quad (5)$$

However, due to the limited number of frames T with respect to the number of pixels K in a patch (several tens), the sample covariance estimator $\hat{\mathbf{S}}_{\theta_k}$ is either rank deficient or displays a prohibitively large variance. Several regularized covariance estimators were compared²³ and the *shrinkage* estimator²⁵ was found to be the most appropriate. Following the work of Y.Chen *et al.*,²⁶ the shrinkage estimator $\hat{\mathbf{C}}_{\theta_k}$ is given by the convex combination:

$$\hat{\mathbf{C}}_{\theta_k} = (1 - \hat{\rho}) \hat{\mathbf{S}}_{\theta_k} + \hat{\rho} \hat{\mathbf{F}}_{\theta_k}, \quad (6)$$

where $\hat{\mathbf{S}}_{\theta_k}$ is the low-bias/high-variance sample covariance matrix given in Eq. (5) and $\hat{\mathbf{F}}_{\theta_k}$ is the high-bias/low-variance diagonal matrix formed from the sample variances. The tradeoff between the two terms of the convex combination is balanced in a data-driven fashion by the estimated factor $\hat{\rho}$:^{23, 26}

$$\hat{\rho}(\hat{\mathbf{S}}_{\theta_k}) = \frac{\text{tr}(\hat{\mathbf{S}}_{\theta_k}^2) + \text{tr}^2(\hat{\mathbf{S}}_{\theta_k}) - 2 \sum_{i=1}^K [\hat{\mathbf{S}}_{\theta_k}]_{ii}^2}{(T+1) \left(\text{tr}(\hat{\mathbf{S}}_{\theta_k}^2) - \sum_{i=1}^K [\hat{\mathbf{S}}_{\theta_k}]_{ii}^2 \right)}, \quad (7)$$

Once the background statistics $(\mathbf{m}_{\theta_k}, \mathbf{C}_{\theta_k})$ are computed, the flux of the potential exoplanet (equation 2) and the GLRT can be expressed by:

$$\begin{cases} \hat{\alpha}^+ = \max(b, 0)/a \\ (\text{GLRT}^+) \quad \frac{\max(b, 0)^2}{a} \underset{\mathcal{H}_0}{\overset{\mathcal{H}_1}{\geq}} \eta. \end{cases} \quad (8)$$

with

$$\begin{cases} a = \sum_{\ell=1}^T \mathbf{h}_{[\phi_{t_\ell}]}(\phi_{t_\ell})^t \cdot \hat{\mathbf{C}}_{[\phi_{t_\ell}]}^{-1} \cdot \mathbf{h}_{[\phi_{t_\ell}]}(\phi_{t_\ell}) \\ b = \sum_{\ell=1}^T \mathbf{h}_{[\phi_{t_\ell}]}(\phi_{t_\ell})^t \cdot \hat{\mathbf{C}}_{[\phi_{t_\ell}]}^{-1} \cdot (\mathbf{r}_{[\phi_{t_\ell}], t_\ell} - \hat{\mathbf{m}}_{[\phi_{t_\ell}]}) \end{cases}, \quad (9)$$

where $\mathbf{h}_{[\phi_{t_\ell}]}(\phi_{t_\ell})$ is the off-axis PSF for a source at subpixelic location ϕ_{t_ℓ} sampled over a patch whose center is $[\phi_{t_\ell}]$, the nearest pixel to ϕ_{t_ℓ} .

We note that when $\eta \geq 0$, the latter test is equivalent to:

$$(\text{SNR}) \quad \hat{\alpha} / \hat{\sigma}_\alpha \underset{\mathcal{H}_0}{\overset{\mathcal{H}_1}{\geq}} \tau \quad (10)$$

where $\hat{\sigma}_\alpha = 1/\sqrt{a}$ is the standard deviation of $\hat{\alpha}$ (see our journal article²³ for details) and $\tau = \sqrt{\eta}$. It can be interpreted as the signal-to-noise ratio (SNR) of the estimation of the flux α of the source. This test follows

a normal distribution with a zero mean and a unit variance so that its thresholding at a given value τ can be directly converted into a probability of false alarm (PFA) and probability of detection (PD):

$$\begin{cases} \text{PFA}(\tau) = \Pr(\hat{\alpha}/\hat{\sigma}_\alpha > \tau | \mathcal{H}_0) = \int_\tau^{+\infty} \frac{1}{\sqrt{2\pi}} \exp\left(-\frac{x^2}{2}\right) dx = 1 - \Phi(\tau) \\ \text{PD}(\tau, \alpha) = \Pr(\hat{\alpha}/\hat{\sigma}_\alpha > \tau | \mathcal{H}_1) = \int_\tau^{+\infty} \frac{1}{\sqrt{2\pi}} \exp\left(-\frac{[x - \alpha/\hat{\sigma}_\alpha]^2}{2}\right) dx = 1 - \Phi(\tau - \alpha/\hat{\sigma}_\alpha) \end{cases}$$

where Φ is the cumulative distribution function of the standard normal distribution. The minimal flux α of a source ensuring its detection with given probabilities of detection PD and false alarm PFA is:

$$\alpha = (\Phi^{-1}(1 - \text{PFA}) - \Phi^{-1}(1 - \text{PD})) \times \hat{\sigma}_\alpha. \quad (11)$$

We have shown²³ on VLT/SPHERE-IRDIS datasets that the probability of false alarm estimated with PACO is reliable, contrary to most of the state-of-the-art methods that produce many more false alarms in practice than theoretically expected.

In the case of an integral field spectrograph with L spectral channels, each wavelength can be processed independently leading to L SNR maps that can be combined. By denoting SNR_λ the SNR at wavelength λ , the combined SNR for $\lambda \in \{1, \dots, L\}$ is:

$$\text{combined-SNR}_{\lambda=1:L} = \sqrt{\sum_{\lambda=1}^L \max(\text{SNR}_\lambda, 0)^2} = \sqrt{\sum_{\lambda=1}^L \text{GLR}_\lambda^+} \quad (12)$$

2.2 Astrometric and Photometric Accuracies

2.2.1 Unbiased Astrometric and Photometric Estimation

In the presence of an exoplanet, the collection of patches $\{\mathbf{r}_{\theta_k, t_\ell}\}_{\ell=1:T}$ used to compute the background statistics around the 2D-location θ_k do not contain pure background but background contaminated by the exoplanet. The resulting flux estimator would be biased should the flux of the background and the flux of the source be estimated separately. An unbiased flux estimation is obtained by joint estimation of the fluxes. In practice, this is done by alternating between the estimation of the background statistics and the estimation of the exoplanet flux. At iteration $n + 1$, after a flux $\hat{\alpha}^{(n)}$ has been estimated assuming background statistics $\hat{\mathbf{C}}^{(n)}$, the background statistics can be improved by computing:

$$\begin{cases} \hat{\mathbf{m}}_{\theta_k}^{(n+1)} = \frac{1}{T} \sum_{\ell=1}^T (\mathbf{r}_{\theta_k, t_\ell} - \hat{\alpha}^{(n)} \mathbf{h}_{\theta_k}(\phi_{t_\ell})) \\ \hat{\mathbf{S}}_{\theta_k}^{(n+1)} = \frac{1}{T} \sum_{\ell=1}^T (\mathbf{r}_{\theta_k, t_\ell} - \hat{\mathbf{m}}_{\theta_k}^{(n+1)}) \cdot (\mathbf{r}_{\theta_k, t_\ell} - \hat{\mathbf{m}}_{\theta_k}^{(n+1)})^t \\ [\hat{\mathbf{F}}_{\theta_k}^{(n+1)}]_{ii} = [\hat{\mathbf{S}}_{\theta_k}^{(n+1)}]_{ii} \\ \hat{\rho}^{(n+1)} = \hat{\rho}(\hat{\mathbf{S}}_{\theta_k}^{(n+1)}) \\ \hat{\mathbf{C}}^{(n+1)} = (1 - \hat{\rho}^{(n+1)}) \hat{\mathbf{S}}^{(n+1)} + \hat{\rho}^{(n+1)} \hat{\mathbf{F}}^{(n+1)}. \end{cases} \quad (13)$$

An unbiased estimation of the position of the source is provided by the maximum likelihood location, which requires to identify the solution of a non-convex optimization problem. We solve this problem by performing an exhaustive search at a finite (subpixel) resolution, refined by a local optimization step. In our forthcoming conference paper,²⁷ each detected source is removed from the data following an orthogonal matching pursuit strategy allowing a complete automatization of the detection and flux estimation steps at a controlled false alarm rate. Contrary to existing approaches,^{13, 16, 17} an unbiased flux estimation is thus obtained without postprocessing or fake companion injections.

2.2.2 Theoretical Analysis of the Astrometric and Photometric Accuracies

Under our statistical model, the astrometric and photometric estimators, based on maximum likelihood estimators, are asymptotically unbiased (i.e., unbiased when the number of measurements tends to infinity). Their accuracy asymptotically reaches the Cramér-Rao lower bounds (CRLBs).²⁴ The standard deviations $\delta_{\theta_k} = \{\delta_\alpha, \delta_{x_0}, \delta_{y_0}\}$ on the estimated parameters $\Omega = \{\alpha, x_0, y_0\}$ (with $\phi_0 = \{x_0, y_0\}$) at the 2D-location θ_k are obtained from the diagonal of the inverse of the Fisher information matrix:

$$[\delta_{\theta_k}]_i = \sqrt{[\mathbf{I}_{\theta_k}^F(\Omega)^{-1}]_{i,i}} \quad \text{with} \quad [\mathbf{I}_{\theta_k}^F(\Omega)]_{i,j} = \frac{\partial \alpha \mathbf{h}_{\theta_k}(\Omega)^t}{\partial \Omega_i} \cdot \mathbf{C}_{\theta_k}^{-1} \cdot \frac{\partial \alpha \mathbf{h}_{\theta_k}(\Omega)}{\partial \Omega_j}. \quad (14)$$

3. APPLICATION OF PACO TO ADI SEQUENCES FROM THE VLT/SPHERE-IRDIS INSTRUMENT

3.1 Datasets Description and Reduction Strategies

In the following, in order to decrease the computational cost of the reduction step using PACO, we use a fast approximate version of our algorithm (algorithm Fast PACO described in our article²³ for more details). The acceleration is based on a precomputation and hard-storage of the terms appearing multiple times in the sums of equations 9 for the different tested positions of the field of view. The results from this fast algorithm can be refined using the complete detection strategy describes in section 2.1 at the cost of an increase of the computational complexity by a factor T . The number K of pixels in a patch should be large enough to encompass the core of the off-axis PSF. Since the PSF varies marginally from one observation to another, K is almost constant for a given instrument, so that PACO is completely parameter-free. For example, we have found using Monte-Carlo injections of fake exoplanets that $K = 49$ pixels in a patch was optimal for SPHERE-IRDIS instrument at $\lambda_1 = 2.110\mu\text{m}$ (K1 Johnson band). We compare the performance of PACO with TLOCI and KLIP standards (see section 1 for a short description) as implemented in the ESO-SPHERE reduction pipeline SpeCal.²⁸ In order to reduce the potential high stellar leakages and the impact of false detections due to defective pixels, SpeCal applies an unsharp filtering as postprocessing on its resulting detections maps. With PACO, no processing (other than the conventional prereduction pipeline⁹) is applied on the science data or on the resulting detection maps.

We illustrate and compare the performance of PACO in terms of detection capability on two ADI datasets from the VLT/SPHERE-IRDIS instrument at $\lambda_1 = 2.110\mu\text{m}$. The observed target is the HD95086 star located in the Carina constellation and hosting a 5-Jovian mass exoplanet (HD95086-b) orbiting about 0.62 arcsecond from its star. This known exoplanet was discovered and confirmed using direct imaging with the SPHERE instrument.^{29,30} The dataset from the first epoch is made of 52 temporal frames acquired under the 2015-05-05 – 095.C-0298(A) ESO program with a total apparent rotation of the field of view of 18.2°. The dataset from the second epoch is made of 80 temporal frames acquired under the 2016-01-17 – 096.C-0241(G) ESO program with a total apparent rotation of the field of view of 28.1°. Since several background faint point sources and background stars are visible in the projected field of view of the instrument, we limit the study to a region of 3.5 arcseconds of radius around the host star. The HD95086-b exoplanet plus two background faint point sources are visible in the considered field of view.

3.2 Signal-to-Noise Maps and Achievable Contrasts

Figure 1 shows the SNR maps obtained with TLOCI, KLIP and PACO algorithms on the two considered datasets. The detections above a conventional threshold at $\tau = 5$ (theoretically leading to $\text{PFA} \leq 2.87 \times 10^{-7}$) are classified as true or false detections. PACO is the only tested algorithm able to detect the three known faint sources without false alarm in the whole field of view. At the first epoch, the fourth highest SNR values from PACO (the first one which is not a real known faint point source) is about 3.6 to compare with 119 for TLOCI and 8.3 for KLIP, emphasizing the ability of PACO to distinguish without ambiguity the faint point sources from the speckles. Contrary to other methods, the detection maps from PACO are also almost stationary even in the vicinity of the host star without postprocessing. KLIP outperforms TLOCI algorithm because the number of false alarms is limited (but still higher than expected at the chosen threshold). However, only one of the three known faint point sources is detected at $\text{SNR} \geq 5$.

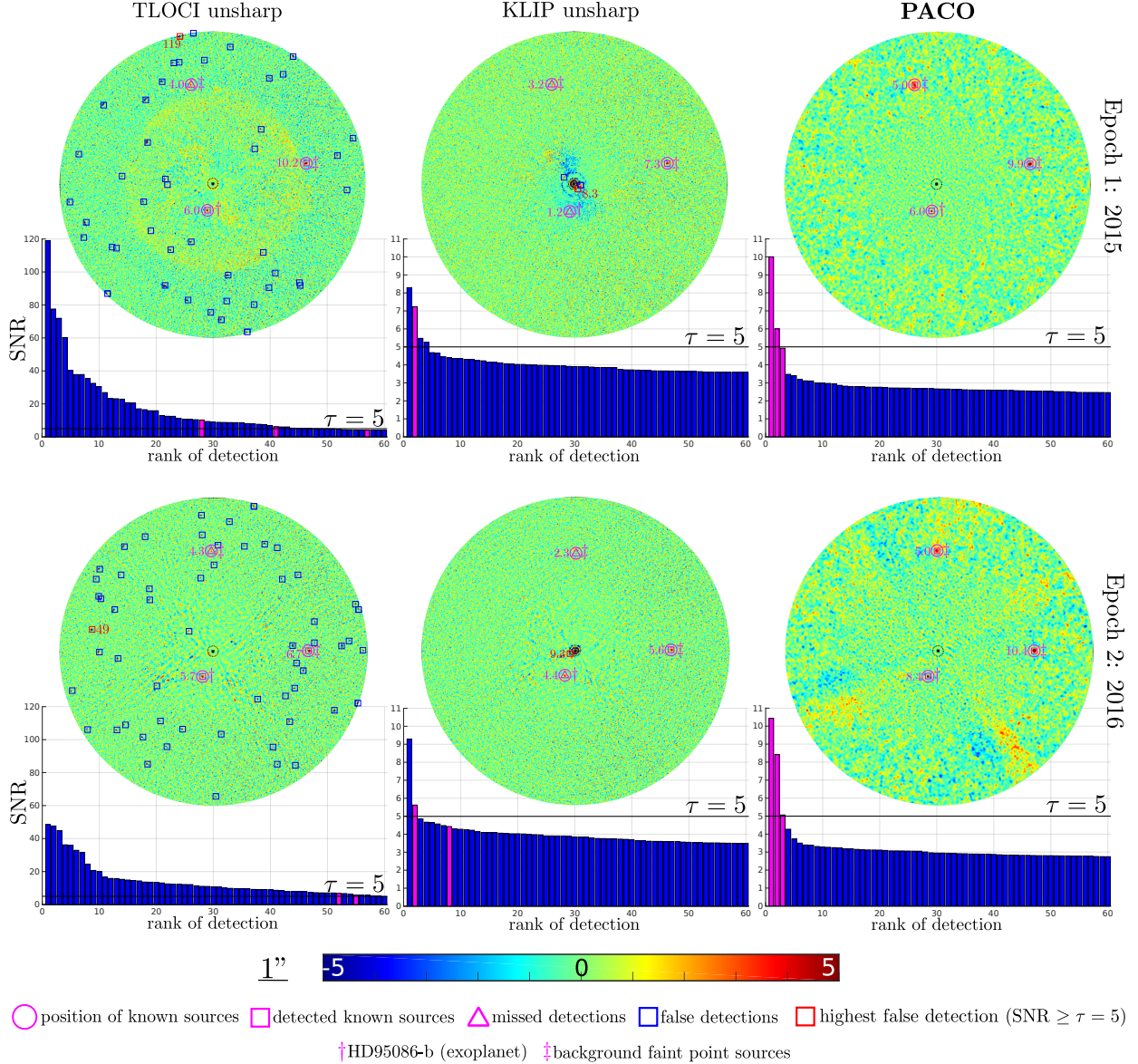


Figure 1. SNR maps obtained with TLOCI, KLIP and PACO algorithms around the HD95086 star at two epochs (2015 and 2016). The detections above a conventional threshold at $\tau = 5$ are classified as true or false detections directly on the SNR maps using square patterns. The 60 first detections are plotted as bar charts below each SNR map, ordered by decreasing SNR values, with true detections in pink (true faint point sources) and false detections in blue.

Equation (11) provides an estimate of the minimum flux of a source required to detect the fraction PD of the total number of sources under a given probability of false alarm. As stated before, the conventional threshold of the SNR maps at $\tau = 5$ corresponds to a probability of alarm $\text{PFA}(\tau = 5) = 2.87 \times 10^{-7}$. Injecting this PFA in equation (11) leads to a minimal contrast $\alpha = 5\sigma_\alpha$ to detect half of the sources. Figure 2 gives the contrast maps for PACO at 5σ for a probability of detection $\text{PD} = 50\%$ for the two considered datasets on the whole field of view. These maps are directly derived from equation (11) so that the contrast is assessed without Monte-Carlo simulations and/or fake exoplanets injections. They emphasize that the contrast at 5σ is not constant throughout the field of view. As expected, it is higher (performance is worse) at smaller separations due to the proximity of the host star. Farther from the host star, some areas are locally less favorable than others due

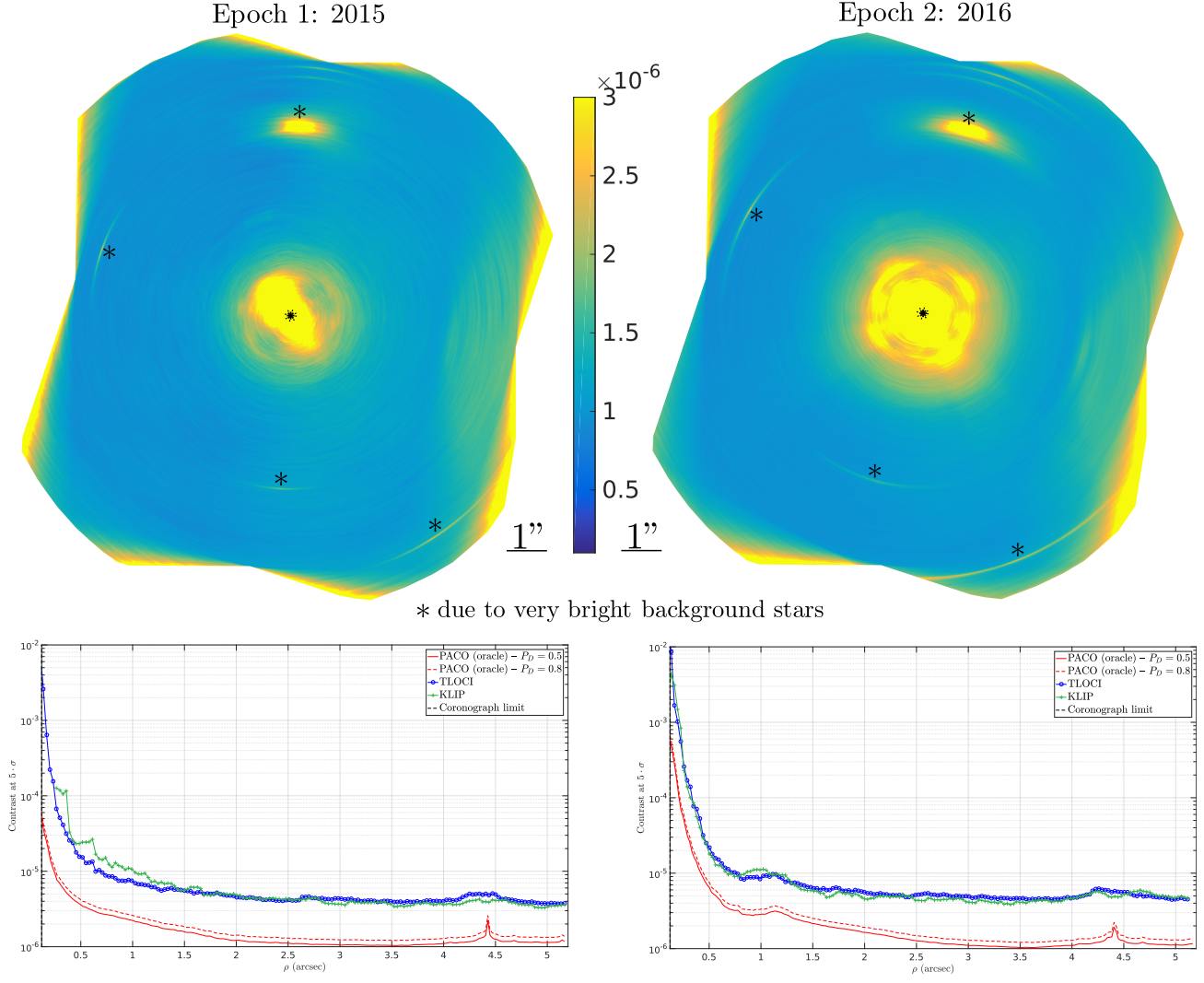


Figure 2. 1st line: PACO contrast maps at 5σ for a probability of detection $PD = 50\%$. 2nd line: Contrast curves at 5σ obtained with PACO, TLOCI and KLIP algorithms. The results are obtained on the HD95086 datasets at the two considered epochs on the whole field of view offered by the SPHERE-IRDIS instrument.

to the presence in the field of view of very bright background stars which are not masked by the coronagraph. Figure 2 also gives contrast curves at 5σ for the different algorithms tested. The contrast curves for PACO are directly derived from equation (11). In practice, they are obtained by performing a radial average of the contrast maps. The achievable contrast with PACO is better than the one from TLOCI and KLIP. We have shown in our article²³ that it is a reliable estimate of the achievable contrast for angular separations higher than 2.5 arcseconds. For shorter angular separations, the actual contrast that can be achieved in practice is worse (typically at the level of contrast obtained for $PD = 80\%$, which is also given in figure 2), since we assume in the derivation of the contrast curves that the background statistics are perfectly known while in practice they must be estimated in the presence of a source. For this reason, we refer to the contrast curves as “oracle” contrast (achievable should an oracle provide the background statistics even in the presence of a source).

Figure 3 gives the CRLB (minimal standard-deviation) maps on the estimated parameters $\Omega = \{\alpha, x_0, y_0\}$ for the two considered datasets. These maps can be directly exploited to predict the standard deviation of the flux estimate and source location. For example, far from the host star, $\{\delta_\alpha, \delta_{x_0}, \delta_{y_0}\} \simeq \{1 \times 10^{-6}, 3 \times 10^{-6}/\alpha \text{ pixels}, 3 \times 10^{-6}/\alpha \text{ pixels}\}$ at the first epoch. It means that the standard-deviation on the flux estimate is

about 1×10^{-6} and about 1 pixel for the localization of a source of flux $\alpha = 3 \times 10^{-6}$. These maps also emphasize that the estimation accuracy is not constant all over the field of view. Particularly, it is worse near very bright sources and telescope spiders.

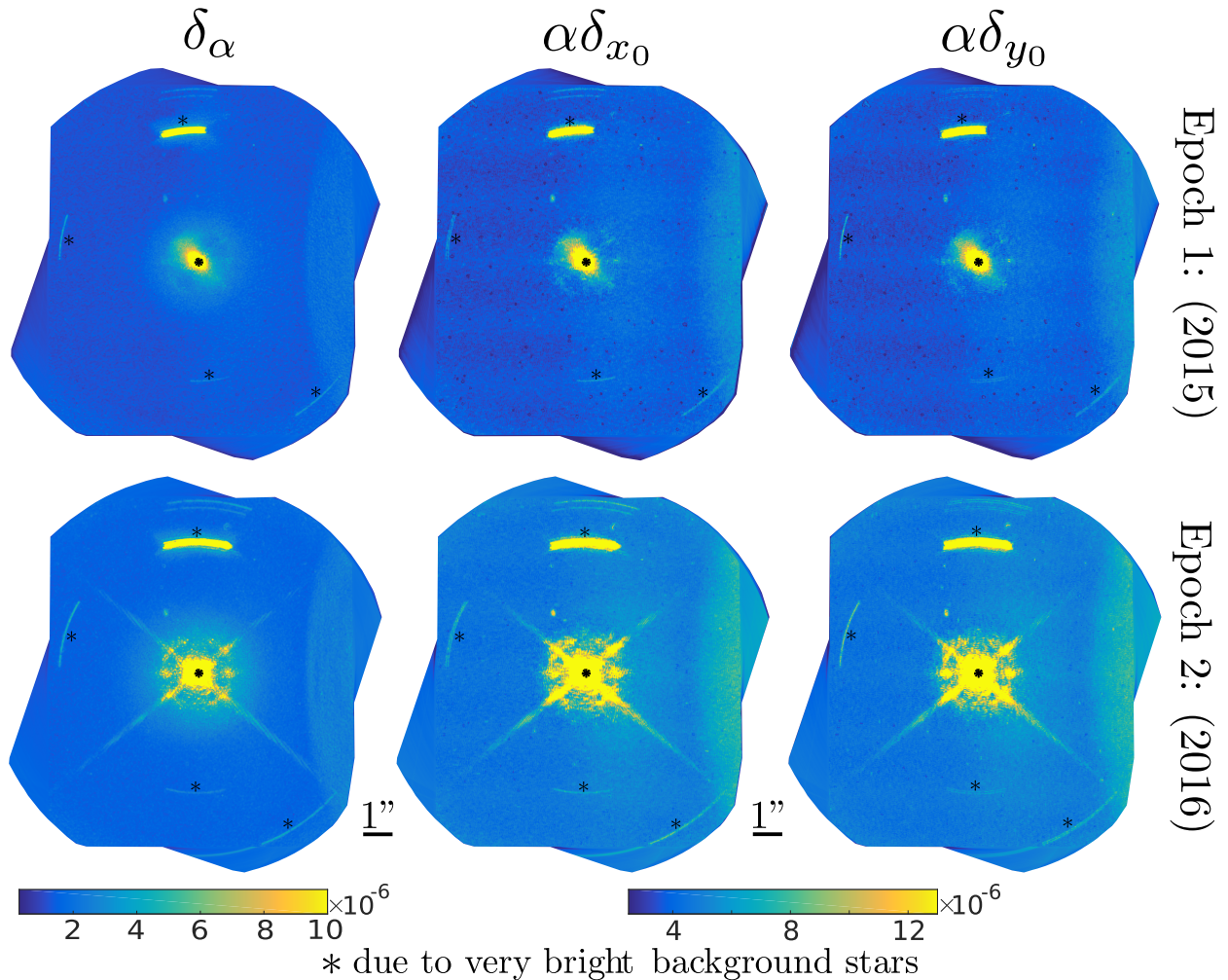


Figure 3. Cramér-Rao lower bounds (minimal standard-deviation) $\delta = \{\delta_\alpha, \delta_{x_0}, \delta_{y_0}\}$ computed on the estimated parameters $\Omega = \{\alpha, x_0, y_0\}$. δ_{x_0} and δ_{y_0} are normalized by the inverse of the flux α of the exoplanet and expressed in pixels unit. The results are obtained on the HD95086 datasets at the two considered epochs on the whole field of view offered by the SPHERE-IRDIS instrument.

A more complete study via additional detection maps, receiver operating curves and contrast curves is conducted in our journal article²³ using injection of faint point sources at challenging level of contrast on others VLT/SPHERE-IRDIS datasets.

4. APPLICATION OF PACO ON ADI+SDI SEQUENCES FROM THE VLT/SPHERE-IFS INSTRUMENT

In this section, we test PACO on multi-spectral datasets from the VLT/SPHERE-IFS instrument. As for TLOCI and KLIP algorithms, each spectral channel is processed independently from the others. A joint spectral processing using PACO would improve the detection limit but requires some refinements which are detailed in a paper in preparation. The tested target is the HR8799 star located in the Pegasus constellation. The star hosts four known exoplanets which were confirmed using direct imaging.³¹ Three of them (HR8799-c-d-e) can

be visible within the field of view offered by the SPHERE-IFS imager. The fourth one (HR8799-b) orbits about 1.72 arcsec from its host star and is outside the SPHERE-IFS field of view. The considered dataset is made of 46 temporal frames acquired under the 2015-07-04 – 095.C-0298(C) ESO program with a total apparent rotation of the field of view of 16.4° .

Figure 4 shows the SNR maps from TLOCI, KLIP, and PACO at the four wavelengths $\lambda = 1.39 \mu\text{m}$, $1.50 \mu\text{m}$, $1.54 \mu\text{m}$ and $1.65 \mu\text{m}$. Figure 5 gives the combined SNR as defined in equation 12 on the $L = 39$ available wavelengths ($0.96 \mu\text{m} \leq \lambda \leq 1.64 \mu\text{m}$) and on the 10 spectral channels part of the H-Johnson band ($1.49 \mu\text{m} \leq \lambda \leq 1.64 \mu\text{m}$) in which the exoplanet signal is the strongest. As in section 3, an unsharp filtering is applied as postprocessing by the SPHERE reduction pipeline on the TLOCI and KLIP SNR maps. At $\lambda = 1.39 \mu\text{m}$, the exoplanetary signal is too weak to be detected by the three tested algorithms. However, PACO is the only tested algorithm producing a stationary map (except near the coronagraph), without false detections since the highest SNR values (corresponding to a speckle) is about 2.8 for PACO to compare with 228 for TLOCI and 7×10^5 for KLIP. The false alarms are particularly important in the corner of the field of view using the tested state-of-the-arts techniques. This is particularly problematic when an exoplanet (such as HR8799-c) is present in this area since it cannot be easily distinguished from the background. PACO seems significantly less sensitive to this kind of effects since aberrant and/or saturated pixels in the science data are considered as missing data in PACO and do not impact the background statistics. Figure 6 illustrates that PACO can lead to the location of exoplanets at a subpixel resolution. In practice, this refinement decreases the residual negative bias on the SNR of a source due to the regular sampling of the criteria grid. We also evaluated the fraction $\mathbb{E}(\text{SNR}(\mathcal{G}_s(\phi_0) | \phi_0)) / \mathbb{E}(\text{SNR}(\phi_0 | \phi_0))$ of SNR lost due to the sampling grid \mathcal{G}_s under consideration, with $\mathcal{G}_s(\phi_0) = \arg \min_{\phi \in \mathcal{G}_s} \|\phi - \phi_0\|^2$, showing that it is unlikely that a faint source be missed due to sampling the SNR map at integer pixel locations rather than at the true subpixel location of the source. Figure 7 gives the contrast maps derived from PACO and the contrast curves from the three tested algorithms. Figure 8 gives the CRLB (minimal standard deviation) maps on the estimated parameters $\Omega = \{\alpha, x_0, y_0\}$ for the four considered wavelengths. It shows that the minimal contrast of a source to be detected at $\text{SNR} = 5$ as well as the astrometric and photometric accuracies depend both on the location and on the spectral channel.

5. CONCLUSION

We illustrated our recent exoplanet detection algorithm PACO on angular differential imaging datasets from the VLT/SPHERE-IRDIS instrument. PACO learns a statistical model of the background capturing the average stellar speckles and the spatial correlations. The decision in favor of the presence or absence of an exoplanet is performed by a binary hypotheses test. PACO differs from the standard reduction algorithms by the absence of differential image subtraction leading to an intrinsically unbiased photometry. PACO is also completely parameter-free and produces stationary detection maps which can be thresholded at a controlled probability of false alarm without any postprocessing step. The expected contrast at 5σ as well as the astrometric and photometric accuracies can be straightforwardly assessed without Monte-Carlo injections. In this paper, we also applied PACO to multi-spectral datasets from the VLT/SPHERE-IFS instrument. Each channel is processed independently and the resulting SNR maps are then combined. A joint processing of the data at different wavelengths is expected to improve the detection maps (in particular, improve the detection limit). This is the subject of on-going work.

ACKNOWLEDGMENTS

This work has been supported by the CNRS through Défi Imag’In project RESSOURCES and the “Programme National de Planétologie” (PNP) of CNRS-INSU cofunded by CNES. This work has made use of the SPHERE Data Center, jointly operated by Osug/Ipag (Grenoble, France), Pytheas/Lam/Cesam (Marseille, France), OCA/Lagrange (Nice, France) and Observatoire de Paris/Lesia (Paris, France).

REFERENCES

- [1] Traub, W. A. and Oppenheimer, B. R., “Direct imaging of exoplanets,” *Exoplanets*, 111–156 (2010).

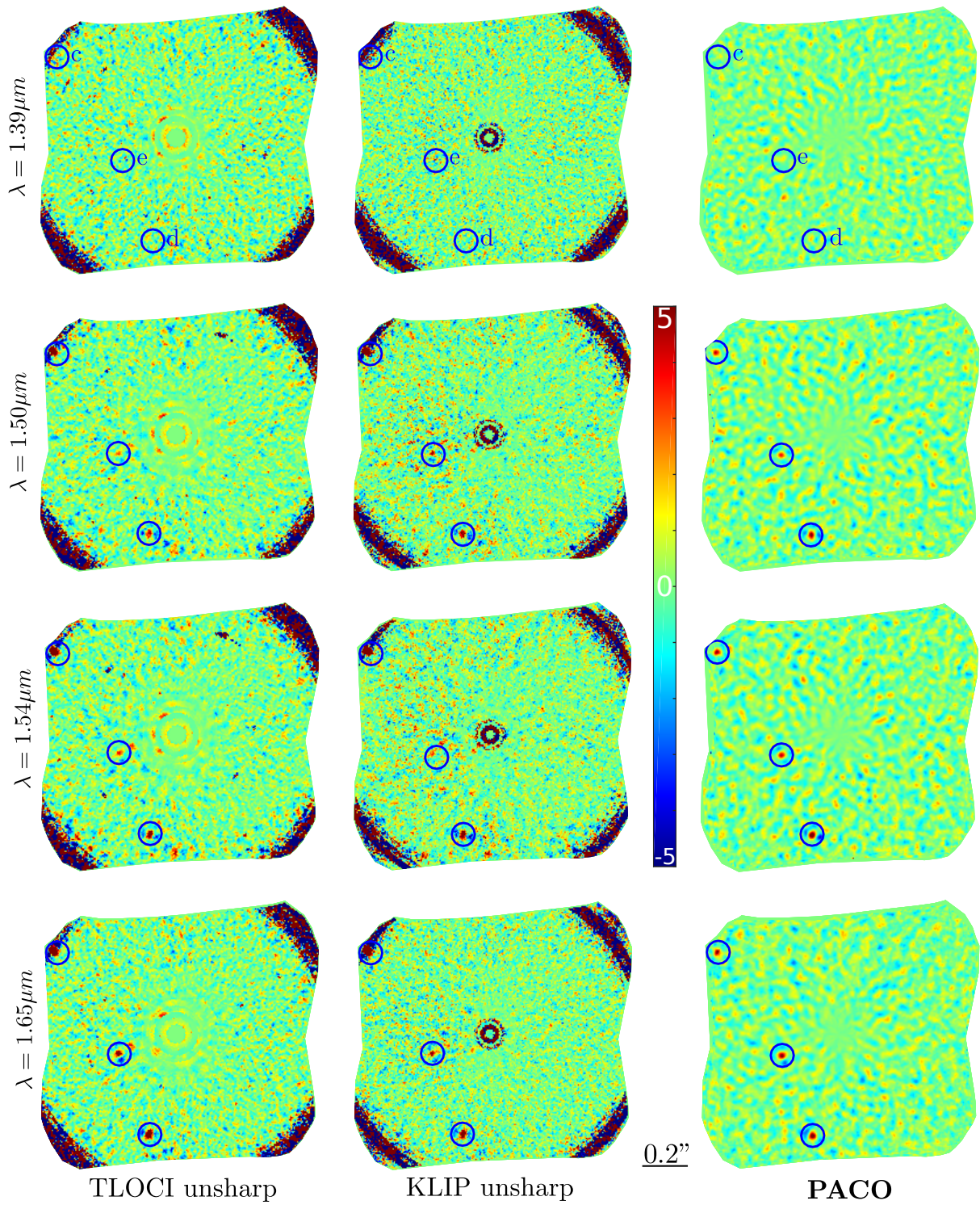


Figure 4. SNR maps obtained with TLOCI, KLIP and PACO algorithms around the HR8799 star with the SPHERE-IFS instrument at $\lambda = 1.39 \mu\text{m}$, $1.50 \mu\text{m}$, $1.54 \mu\text{m}$ and $1.65 \mu\text{m}$. The expected positions of the three known exoplanets are marked by blue circles.

- [2] Vigan, A., Moutou, C., Langlois, M., Allard, F., Boccaletti, A., Carbillet, M., Mouillet, D., and Smith, I., “Photometric characterization of exoplanets using angular and spectral differential imaging,” *Monthly Notices of the Royal Astronomical Society* **407**(1), 71–82 (2010).
- [3] Kuzuhara, M., Tamura, M., Kudo, T., Janson, M., Kandori, R., Brandt, T., Thalmann, C., Spiegel, D., Biller, B., Carson, J., et al., “Direct imaging of a cold jovian exoplanet in orbit around the sun-like star gj 504,” *The Astrophysical Journal* **774**(1), 11 (2013).
- [4] Bonavita, M., Daemgen, S., Desidera, S., Jayawardhana, R., Janson, M., and Lafrenière, D., “A new substellar companion around the young star hd 284149,” *The Astrophysical Journal Letters* **791**(2), L40 (2014).
- [5] Soummer, R., “Apodized pupil lyot coronagraphs for arbitrary telescope apertures,” *The Astrophysical Journal Letters* **618**(2), L161 (2004).
- [6] Mawet, D., Riaud, P., Baudrand, J., Baudoz, P., Boccaletti, A., Dupuis, O., and Rouan, D., “The four-quadrant phase-mask coronagraph: white light laboratory results with an achromatic device,” *Astronomy & Astrophysics* **448**(2), 801–808 (2006).
- [7] Beuzit, J.-L., Feldt, M., Dohlen, K., Mouillet, D., Puget, P., Wildi, F., Abe, L., Antichi, J., Baruffolo, A., Baudoz, P., et al., “Sphere: a planet finder instrument for the vlt,” in [*Ground-based and airborne instrumentation for astronomy II*], **7014**, 701418, International Society for Optics and Photonics (2008).
- [8] Dohlen, K., Langlois, M., Saisse, M., Hill, L., Origne, A., Jacquet, M., Fabron, C., Blanc, J.-C., Llored, M., Carle, M., et al., “The infra-red dual imaging and spectrograph for sphere: design and performance,” in [*Ground-based and Airborne Instrumentation for Astronomy II*], **7014**, 70143L, International Society for Optics and Photonics (2008).
- [9] Pavlov, A., Möller-Nilsson, O., Feldt, M., Henning, T., Beuzit, J.-L., and Mouillet, D., “Sphere data reduction and handling system: overview, project status, and development,” in [*Advanced Software and Control for Astronomy II*], **7019**, 701939, International Society for Optics and Photonics (2008).
- [10] Racine, R., Walker, G. A., Nadeau, D., Doyon, R., and Marois, C., “Speckle noise and the detection of faint companions,” *Publications of the Astronomical Society of the Pacific* **111**(759), 587 (1999).
- [11] Marois, C., Lafreniere, D., Doyon, R., Macintosh, B., and Nadeau, D., “Angular differential imaging: a powerful high-contrast imaging technique,” *The Astrophysical Journal* **641**(1), 556 (2006).
- [12] Lafreniere, D., Marois, C., Doyon, R., Nadeau, D., and Artigau, É., “A new algorithm for point-spread function subtraction in high-contrast imaging: a demonstration with angular differential imaging,” *The Astrophysical Journal* **660**(1), 770 (2007).
- [13] Marois, C., Correia, C., Véran, J.-P., and Currie, T., “Tloci: A fully loaded speckle killing machine,” *Proceedings of the International Astronomical Union* **8**(S299), 48–49 (2013).
- [14] Marois, C., Correia, C., Galicher, R., Ingraham, P., Macintosh, B., Currie, T., and De Rosa, R., “Gpi psf subtraction with tloci: the next evolution in exoplanet/disk high-contrast imaging,” in [*Adaptive Optics Systems IV*], **9148**, 91480U, International Society for Optics and Photonics (2014).
- [15] Currie, T., Debes, J., Rodigas, T. J., Burrows, A., Itoh, Y., Fukagawa, M., Kenyon, S. J., Kuchner, M., and Matsumura, S., “Direct imaging confirmation and characterization of a dust-enshrouded candidate exoplanet orbiting fomalhaut,” *The Astrophysical Journal Letters* **760**(2), L32 (2012).
- [16] Wahhaj, Z., Cieza, L. A., Mawet, D., Yang, B., Canovas, H., De Boer, J., Casassus, S., Ménard, F., Schreiber, M. R., Liu, M. C., et al., “Improving signal-to-noise in the direct imaging of exoplanets and circumstellar disks with mloci,” *Astronomy & Astrophysics* **581**, A24 (2015).
- [17] Soummer, R., Pueyo, L., and Larkin, J., “Detection and characterization of exoplanets and disks using projections on karhunen-loève eigenimages,” *The Astrophysical Journal Letters* **755**(2), L28 (2012).
- [18] Gonzalez, C. G., Absil, O., Absil, P.-A., Van Droogenbroeck, M., Mawet, D., and Surdej, J., “Low-rank plus sparse decomposition for exoplanet detection in direct-imaging adi sequences-the llsg algorithm,” *Astronomy & Astrophysics* **589**, A54 (2016).
- [19] Eggenberger, A., Cornia, A., Mugnier, L., Mouillet, D., Chauvin, G., Boccaletti, A., and Rousset, G., “Testing the andromeda method for exoplanet detection on vlt/naco data,” in [*In the Spirit of Lyot 2010*], (2010).

- [20] Cantalloube, F., Mouillet, D., Mugnier, L., Milli, J., Absil, O., Gonzalez, C. G., Chauvin, G., Beuzit, J.-L., and Cornia, A., “Direct exoplanet detection and characterization using the andromeda method: Performance on vlt/naco data,” *Astronomy & Astrophysics* **582**, A89 (2015).
- [21] Smith, I., Ferrari, A., and Carbillet, M., “Detection of a moving source in speckle noise. application to exoplanet detection,” *IEEE Transactions on Signal Processing* **57**(3), 904–915 (2009).
- [22] Gonzalez, C. A. G., Absil, O., and Van Droogenbroeck, M., “Supervised detection of exoplanets in high-contrast imaging sequences,” *arXiv preprint arXiv:1712.02841* (2017).
- [23] Flasseur, O., Denis, L., Thiébaud, É., and Langlois, M., “Exoplanet detection in angular differential imaging by statistical learning of the nonstationary patch covariances,” *accepted in Astronomy & Astrophysics* (2018).
- [24] Kay, S. M., “Fundamentals of statistical signal processing, vol. ii: Detection theory,” *Signal Processing. Upper Saddle River, NJ: Prentice Hall* (1998).
- [25] Ledoit, O. and Wolf, M., “A well-conditioned estimator for large-dimensional covariance matrices,” *Journal of multivariate analysis* **88**(2), 365–411 (2004).
- [26] Chen, Y., Wiesel, A., Eldar, Y. C., and Hero, A. O., “Shrinkage algorithms for mmse covariance estimation,” *IEEE Transactions on Signal Processing* **58**(10), 5016–5029 (2010).
- [27] Flasseur, O., Denis, L., Thiébaud, E., and Langlois, M., “An unsupervised patch-based approach for exoplanet detection by direct imaging,” in [*IEEE ICIP*], (Oct. 2018).
- [28] Galicher, R., Boccaletti, A., Mesa, D., Delorme, P., Gratton, R., Langlois, M., Lagrange, A.-M., Maire, A.-L., Le Coroller, H., Chauvin, G., Biller, B., Cantalloube, et al., “Astrometric and photometric accuracies in high contrast imaging: The SPHERE speckle calibration tool (SpeCal),” *ArXiv e-prints* (May 2018).
- [29] Rameau, J., Chauvin, G., Lagrange, A.-M., Boccaletti, A., Quanz, S. P., Bonnefoy, M., Girard, J., Delorme, P., Desidera, S., Klahr, H., et al., “Discovery of a probable 4-5 jupiter-mass exoplanet to hd 95086 by direct imaging,” *The Astrophysical Journal Letters* **772**(2), L15 (2013).
- [30] Rameau, J., Chauvin, G., Lagrange, A.-M., Meshkat, T., Boccaletti, A., Quanz, S., Currie, T., Mawet, D., Girard, J., Bonnefoy, M., et al., “Confirmation of the planet around hd 95086 by direct imaging,” *The Astrophysical Journal Letters* **779**(2), L26 (2013).
- [31] Marois, C., Macintosh, B., Barman, T., Zuckerman, B., Song, I., Patience, J., Lafrenière, D., and Doyon, R., “Direct imaging of multiple planets orbiting the star hr 8799,” *Science* **322**(5906), 1348–1352 (2008).

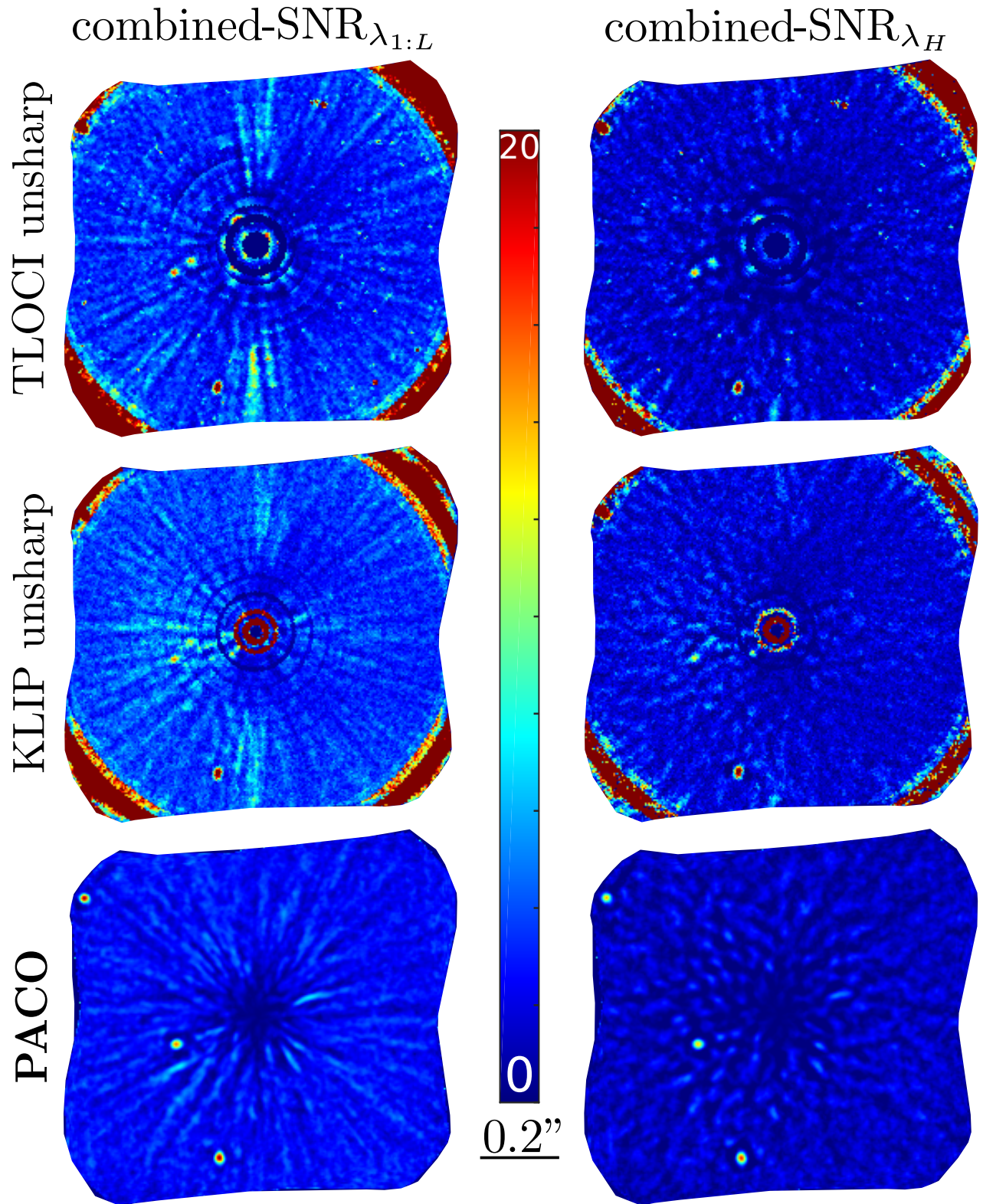


Figure 5. Combined-SNR maps obtained with TLOCI, KLIP and PACO algorithms around the HR8799 star with the SPHERE-IFS instrument. 1st column: the $L = 39$ spectral channels are combined ($\lambda \in \{0.96; 1.64\}\mu\text{m}$). 2nd column: only the 10 available spectral channels part of the H-Johnson band are combined ($\lambda \in \{1.49; 1.64\}\mu\text{m}$).

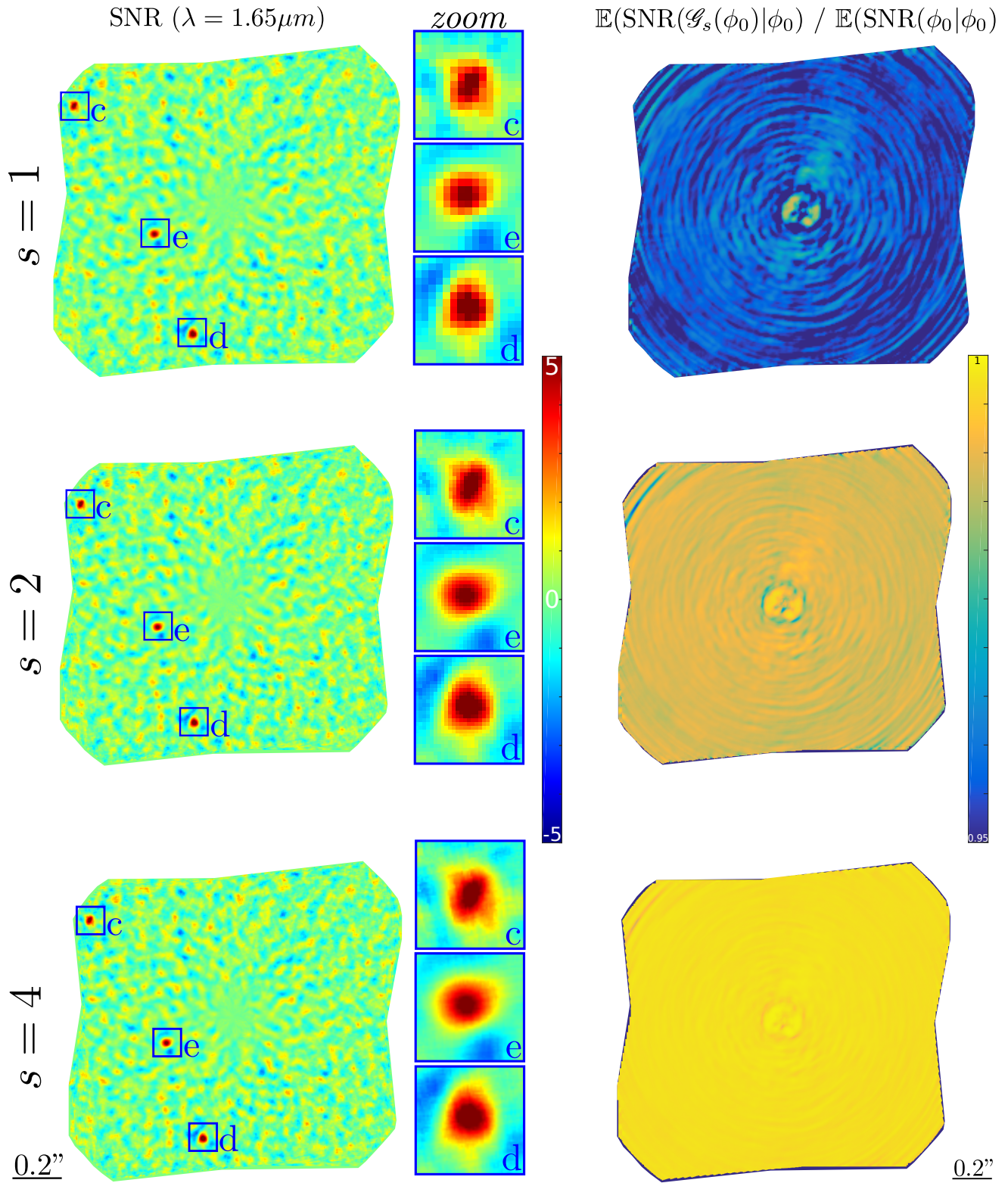


Figure 6. SNR maps from PACO obtained at $\lambda = 1.64\mu\text{m}$ around the HR8799 star. The maps are computed by evaluating the detection criteria on the original pixel grid (corresponding to $s = 1$), and by considering a subpixel resolution by a factor $s = 2$ and $s = 4$.

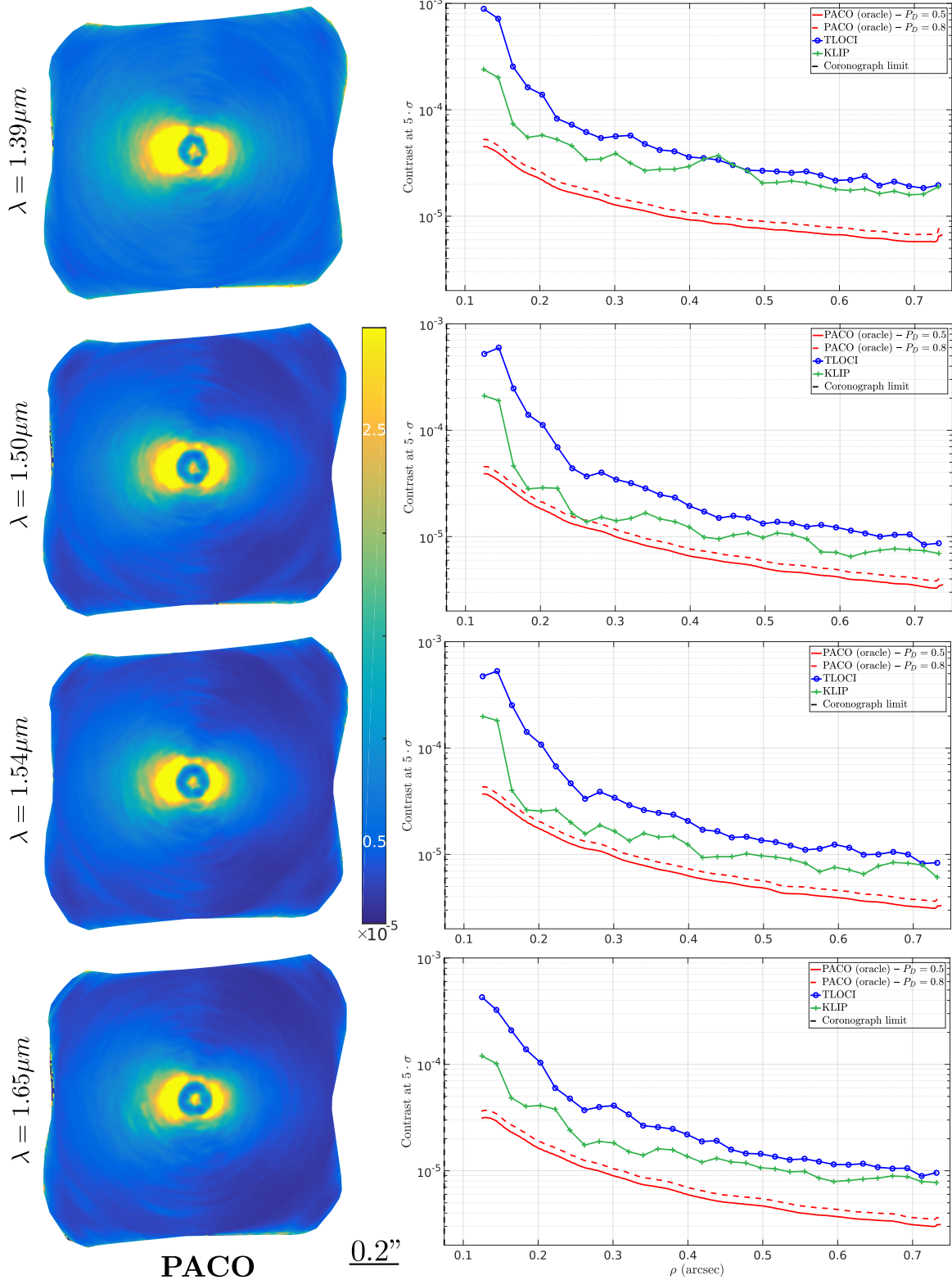


Figure 7. Left: PACO contrast maps at 5σ for a probability of detection $P_D = 50\%$. Right: Contrast curves at 5σ obtained with PACO, TLOCI and KLIP algorithms. The results are obtained around the HR8799 star for the wavelengths $\lambda \in \{1.39; 1.50; 1.54; 1.65\}\mu\text{m}$.

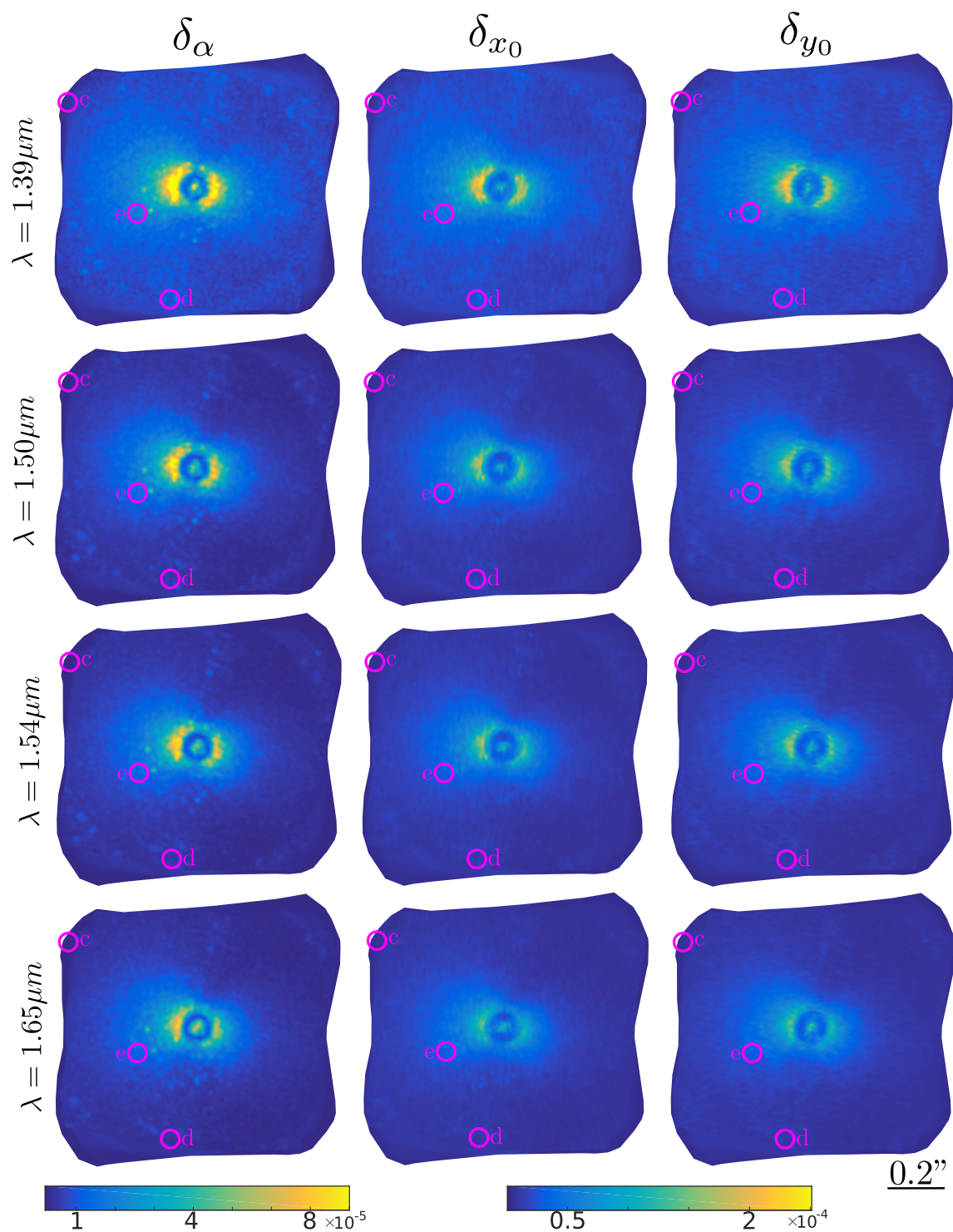


Figure 8. Cramér-Rao lower bounds (minimal standard-deviation) $\delta = \{\delta_\alpha, \delta_{x_0}, \delta_{y_0}\}$ computed on the estimated parameters $\Omega = \{\alpha, x_0, y_0\}$. δ_{x_0} and δ_{y_0} are normalized by the inverse of the flux α of the exoplanet and expressed in pixels unit. The results are obtained on the HR8799 dataset at $\lambda \in \{1.39; 1.50; 1.54; 1.65\} \mu\text{m}$.